A T-Matrix Many-Particle Theory for Low-Dimensional Semiconductor Optics.

M.F. Pereira Jr.[a], T. Schmielau[b], R. Schepe[b] and K. Henneberger[b]

[a] Instituto de Fisica, Universidade Federal da Bahia, 40210-340 Salvador, Bahia, Brazil.

[b] Fachbereich Physik, Universitaet Rostock, 18051, Rostock Germany

ABSTRACT

In low-dimensional systems, quantum-confinement and bandstructure effects strongly influence the many-particle effects that ultimately give rise to the nonlinear optical properties of semiconductores. In this paper, we use a Keldysh Green's functions approach to obtain numerical results for isolated quantum wells and coupled superlattices, and investigate in different limits the combination of band-structure and many-particle effects. The inclusion of higher order Coulomb correlations gives rise to deviations from the results found in the literature for low carrier densities and temperatures, which increase with the fundamental band gap, and may be relevant for future optical device design and operation. The optical spectra presented illustrate the theoretical approach and provide insight on the physical mechanisms responsible for lasing in wide-band gap heterostructures, as contrasted to the usual III-V systems.

Keywords: Many-Body Effects; T-Matrix; Nonlinear Absorption and Gain Low-Dimensional Semiconductors

1. INTRODUCTION

Coulomb effects are now well established as the origin of the near band-gap optical nonlinearities semiconductors.[1,2] In low-dimensional systems, quantum-confinement and non-parabolic bandstructure effects add a further complication for the computation of realistic optical spectra.[3] As the temperature is reduced, and the effective Coulomb interaction between charged carriers increases, even more importantly in systems designed to enhance those effects, like large band-gap, low dimensional semiconductors, many-particle corrections of increasingly higher order are required to explain the electronic and highly non-linear optical properties of such systems. Corrections beyond the Random Phase Approximation (RPA) must be considered.[4,5] In this paper, we use a Keldysh Green's functions formalism that allows for the (self-) consistent inclusion of higher order Coulomb correlations by means of T-matrix diagrams. We show under which conditions the T-matrix leads to deviations in the selfenergies that characterize the relevant quasi-particles of the system. The paper is organized as follows: In Section 2 we summarize the main non-equilibrium Green's functions expressions. In Section 3 we briefly describe how the dephasing is computed. Numerical results for both isolated quantum wells and coupled superlattices are presented in Section 4, which is closed by a brief summary.

2. NON-EQUILIBRIUM GREEN'S FUNCTIONS EXPRESSIONS

The interacting quasi-particles which describe the Semiconductor media in our Keldysh Greens function approach, Namely, carriers (G), photons (D), and plasmons (W),[6] have their time-dependence dictated by Dyson equations (sum over repeated indices is assumed),

$$\left[G^{-1}_{o,ac}(1\underline{3}) - \Sigma_{ac}(1\underline{3})\right] G_{cb}(\underline{3}\,\underline{2}) = \delta_{ab}(1\,\underline{2}), \tag{1}$$

$$\left[D^{-1}_{o}(1\underline{3}) - P(1\underline{3})\right] D(\underline{3}\,\underline{2}) = \hat{\delta}(1\,\underline{2}), \tag{2}$$

$$\left[W^{-1}_{o}(1\underline{3}) - p(1\underline{3})\right] W(\underline{3}\,\underline{2}) = \delta(1\,\underline{2}), \tag{3}$$

or equivalently,

$$D(1\,\underline{2}) = D_o(1\,\underline{2}) + D_o(1\,\underline{4})\, P(\underline{4}\,\underline{3})\, D(\underline{3}\,\underline{2}), \tag{4}$$

$$G_{ab}(1\,\underline{2}) = G_{o,ab}(1\,\underline{2}) + G_{o,ac}(1\,\underline{4})\, \Sigma_{cd}(\underline{4}\,\underline{3})\, G_{db}(\underline{3}\,\underline{2}), \tag{5}$$

$$W(1\,\underline{2}) = V(1\,\underline{2}) + V(1\,\underline{4})\, p(\underline{43})\, W(\underline{3}\,\underline{2}), \tag{6}$$

(Send correspondence to M.F.P)
M.F.P. E-mail: mauro@physik.uni-bremen.de

where $\hat{\delta}$ is the transverse delta function. The labels $a, b, c...$ denote generically the several conduction and valence subbands. The bare Coulomb potential is diagonal in the time indices, $V(\underline{1}\,\underline{2}) = 1/|\vec{R}_1 - \vec{R}_2|\ \delta(t_{\underline{1}} - t_{\underline{2}})$. The inverse free propagators G_o^{-1}, D_o^{-1}, W_o^{-1}, are given by

$$G^{-1}_{o,ab}(\underline{1}\,\underline{2}) = \left[i\hbar\frac{\partial}{\partial t_{\underline{1}}} - h_{eff}(\underline{1})\right]\delta(\underline{1}\,\underline{2}), \tag{7}$$

$$W_o^{-1}(\underline{1}\,\underline{2}) = -\frac{\epsilon_o}{4\pi e^2}\,\triangle_1\,\delta(\underline{1}\,\underline{2}), \tag{8}$$

$$D_o^{-1}(\underline{1}\,\underline{2}) = \left[\triangle_1 - 1/c^2\partial^2/\partial t_{\underline{1}}^2\right]\delta(\underline{1}\,\underline{2}). \tag{9}$$

Here ϵ_o is the static dielectric function. The effective one-particle Hamiltonian in the equation for the free carrier propagator reads,

$$h_{eff}(\underline{1}) = [H_o(\underline{1}) + \Phi_{eff}(\underline{1})]\ \delta_{ab} + \frac{ei\hbar}{cm_o}\vec{A}_{eff}(\underline{1})\cdot\nabla(\underline{1}), \tag{10}$$

where, Φ_{eff} and $\vec{A}_{eff}$ denote, respectively the expectation values of the scalar and vector potentials.

The self-energies, Σ, P, and p denote, respectively, the carrier self-energy, the transverse, and the longitudinal polarization functions. Detailed band-structure and quantum-confinement effects are included in the theory through the term h_{eff} in the free-carrier propagator G_o^{-1}, and also in the optical transition selection rules described by the matrix elements of the velocity operator, $\vec{\Pi}(\underline{1}\,\underline{2}) = (\vec{\Pi}(\underline{1}) + \vec{\Pi}^*(\underline{2}))/2 = \hbar(\nabla(1) - \nabla(2))/2im_o$. The carrier self-energy Σ leads to bandgap renormalization, includes dynamic effects such as corrections beyond Hartree-Fock, scattering rates in the carrier's kinetics, and enables the description of bound states (excitons) in the spectral density of carriers, defining the degree of ionization. The longitudinal polarization function p is responsible for (plasmon) screening of the Coulomb interaction. Furthermore, it describes dynamical screening, screening by excitons, plasmon kinetics and the build up of screening, although, these topics will not be addressed in this paper. The transverse polarization function P yields the excitation dependent absorption coefficient and refractive index, and defines scattering rates (generation/recombination, respectively absorption/emission) in the photon kinetics. It is responsible for the inclusion of bound states (excitons) in the photons spectral density.
Functional derivative or diagammatic techniques allow the consideration of increasingly higher order Coulomb corrections in the self-energies. In this paper, we consider T-matrix correlation contributions (c) beyond the Random Phase Approximation (RPA). For the carrier and photon self-energies, we obtain,[4,5]

$$\Sigma_{aa}(\underline{1}\,\underline{1}') = \Sigma^{HF}_{aa}(\underline{1}\,\underline{1}') + \Sigma^{c}_{aa}(\underline{1}\,\underline{1}'), \tag{11}$$

$$\Sigma^{HF}_{aa}(\underline{1}\,\underline{1}') = -i\hbar\ e^2 G(\underline{1}\,\underline{2})\ W(\underline{2}\,\underline{1}), \tag{12}$$

$$\Sigma^{c}_{aa}(\underline{1}\,\underline{1}') = -i\ T"_{eb}(\underline{1}\,\underline{4}\,\underline{1}'\,\underline{5})\ G(\underline{5}\,\underline{4}) \tag{13}$$

$$\mathcal{P}_{eh}(\underline{1}\,\underline{2}) = \mathcal{P}_{0,eh}(\underline{1}\,\underline{2}) - \hbar\ G_{ee}(\underline{1}\,\underline{3})\ G_{hh}(\underline{1}\,\underline{4})\ T_{eh}(\underline{3}\,\underline{4}\,\underline{5}\,\underline{6})\ G_{ee}(\underline{5}\,\underline{2})\ G_{hh}(\underline{6}\,\underline{2}), \tag{14}$$

where we have introduced the electron-hole quantity,

$$\mathcal{P}_{0,eh}(\underline{1}\,\underline{1}'\,\underline{2}\,\underline{2}') = -i\hbar\ G_{ee}(\underline{1}\,\underline{2})\ G_{hh}(\underline{1}'\,\underline{2}'), \tag{15}$$

The T-matrix,

$$W_{eh}(\underline{3}\,\underline{4})\ \mathcal{P}_{eh}(\underline{3}\,\underline{4}\,\underline{2}\,\underline{2}') = i\hbar\, T_{eh}(\underline{3}\,\underline{4}\,\underline{5}\,\underline{6})\ G_{ee}(\underline{5}\,\underline{2})\ G_{hh}(\underline{6}\,\underline{2}'). \tag{16}$$

satisfies the equation,

$$T_{eh}(\underline{1}\,\underline{2}\,\underline{1}'\,\underline{2}') = W_{eh}(\underline{1}\,\underline{2})\ \delta(\underline{1}\,\underline{1}')\ \delta(\underline{2}\,\underline{2}') + i\,W_{eh}(\underline{1}\,\underline{2})\ G_{ee}(\underline{1}\,\underline{3})\ G_{hh}(\underline{1}'\,\underline{4})\ T_{ab}(\underline{3}\,\underline{4}\,\underline{1}'\,\underline{2}'). \tag{17}$$

The transverse and longitudinal polarization functions are connected By the relation,

$$P_{ab}(12) = \frac{4\pi e^2}{c^2}\vec{\pi}(11^{\pm})\pi(\vec{2})p(11^{\pm}2). \tag{18}$$

3. DEPHASING

The possibility of computing the dephasing and the corresponding bandgap shift that follows by Kramers-Kronig allows for further predictability in the theory, in contrast with a previous approach where fit formulas have been used.[3] They appear directly in the spectral function, $\hat{G}$ which enter in all equations presented above. After suitable Fourier-transformations,

$$\hat{G}_{nn}(k,\omega) = \frac{2\hbar\Gamma_n}{(\hbar\omega - \hbar e_n)^2 + \hbar^2\Gamma_n^2}, \tag{19}$$

where $\hbar e_n = \hbar\epsilon_n - Re\{\Sigma^r_{nn}(k,\omega)\}$, and $\hbar\Gamma_n = -Im\{\Sigma^r_{nn}(k,\omega)\}$ denote, respectively, the renormalized energies and the dephasing rate. The correlation functions are given by

$$G^{>}_{nn} = \hat{G}_{nn}(\vec{k},\omega)\, f^{>}_{n}(\omega),, \tag{20}$$

and $f^{<}_n(\omega)$ is a Fermi function. Algebric manipulations lead to the RPA dephasing,

$$\Gamma_n(\vec{k},\omega) = -2\sum_{\vec{q}} \int_{-\infty}^{\infty} \frac{d\Omega}{2\pi} \Big[n_B(\Omega) + f_n(\omega+\Omega) \Big] \times \hat{G}_{nn}(\vec{k}+\vec{q},\omega+\Omega)\, Im\, \Big[W_{nn}(\vec{k},\omega) \Big], \tag{21}$$

where $n_B(\Omega)$ is the Bose distribution function. Using the Kramers–Kronig relation the real part of the retarded one–particle self-energy Σ^{ret}_{nn} is given by

$$Re\Sigma^{ret}_{nn}(\vec{k},\omega) = P\int_{-\infty}^{\infty} \frac{d\,\Omega}{2\,\pi}\, \frac{\Gamma_n(\vec{k},\Omega)}{\omega - \Omega}, \tag{22}$$

where $P\int$ denotes a Cauchy-type principle value integral. Using the Optical Theorem for the retarded screened potential,

$$Im\, \Big[W_{nn}(\vec{k},\omega) \Big] = \Big| W_{nn}(\vec{k},\omega) \Big|^2\, Im\, \Big[\pi^{ret}_{nn}(\vec{k},\omega) \Big], \tag{23}$$

together with the retarded longitudinal polarization function, π^{ret}_{nn},

$$\pi^{ret}_{nn}(\vec{k},\omega) = -\sum_{\vec{q}} \int_{-\infty}^{\infty} \frac{d\,\omega_1}{2\pi} \int_{-\infty}^{\infty} \frac{d\,\omega_2}{2\pi}\, \hat{G}_{nn}(\vec{q},\omega_1)\, \hat{G}_{nn}(\vec{q}+\vec{k},\omega_2)\, \frac{f_\alpha(\omega_1) - f_\alpha(\omega_2)}{\omega - \omega_1 - \omega_2 + i\delta}, \tag{24}$$

the selfenergies can be computed iteratively together with the corresponding quasi-chemical potentials, which characterize the distribution functions. In order to understand the full process and make a connection to less advanced iteration schemes, note that, the average number of particles in a system of particles of type a (electrons or holes) reads

$$N_a = \int < \Psi^{\dagger}_a(R)\, \Psi_a(R) > \, dR, \tag{25}$$

which can be written as,

$$N_a = -i\hbar \sum_{n_1\vec{k}} \int \frac{d\omega}{2\pi}\, G^{<}_{n_1n_1}(k,\omega) = -i\hbar \sum_{n_1\vec{k}} \int \frac{d\omega}{2\pi}\, \hat{G}_{n_1n_1}(k,\omega)\, f_a(\omega) \tag{26}$$

$$= \sum_{n\vec{k}} \int \frac{d(\hbar\omega)}{2\pi}\, \frac{2\hbar\Gamma_n}{(\hbar\omega - \hbar e_n(k)^2 + \hbar^2\Gamma_n^2}\, f_a(\omega), \tag{27}$$

In the quasi-particle approximation, $\hbar\Gamma_n(k) \to 0$, we obtain the usual (spin summation is included in the subscript n),

$$N_a = \sum_{n\vec{k}} f_a(e_n(k)). \tag{28}$$

At this point we include higher-order T-matrix corrections, following the prescription presented in the previous section. We must then include the terms below in the iterative scheme. The Fourier-transformed ladder or correlation T-Matrix self energy, has forwards and backwards Keldysh components given by

$$\Sigma^{c,\gtrless}_{aa}(\mathbf{p}_1,\omega) = -i\sum_b (2s_b{+}1)\sum_{\mathbf{p}_2}\int \frac{d\omega'}{2\pi}\, T''^{\gtrless}_{ab}(\mathbf{p},\mathbf{p},\mathbf{P},\omega{+}\omega')\cdot G^{\lessgtr}_b(\mathbf{p}_2,\omega')\,, \tag{29}$$

For the cases in which effective masses can be defined, as in the superlattice data presented in section 4, $\mathbf{p} = m_b/(m_a+m_b)\,\mathbf{p}_1 - m_a/(m_a+m_b)\,\mathbf{p}_2$, and $\mathbf{P} = \mathbf{p}_1 + \mathbf{p}_2$.
The Fourier-transformed T-Matrix, $T^{\rm ret}_{ab}(\mathbf{p},\mathbf{p}',\mathbf{P},\omega)$, satisifies the Bethe-Salpeter equation,

$$T^{\rm ret}_{ab}(\mathbf{p},\mathbf{p}',\mathbf{P},\omega) = V_{ab}(\mathbf{p}{-}\mathbf{p}') + \sum_{\bar{\mathbf{p}}} V_{ab}(\mathbf{p}{-}\bar{\mathbf{p}})\cdot \mathcal{G}^{\rm ret}_{ab}(\bar{\mathbf{p}},\mathbf{P},\omega)\cdot T^{\rm ret}_{ab}(\bar{\mathbf{p}},\mathbf{p}',\mathbf{P},\omega), \tag{30}$$

where the uncorrelated two-particle Green's function $\mathcal{G}$, reads

$$\mathcal{G}^{\gtrless}_{ab}(\mathbf{p},\mathbf{P},\omega) = i\int \frac{d\omega'}{2\pi}\, G^{\gtrless}_a(\mathbf{p}_1,\omega{-}\omega')\cdot G^{\gtrless}_b(\mathbf{p}_2,\omega') \tag{31}$$

4. NUMERICAL RESULTS AND DISCUSSION

In this section, we apply our theory for both isolated quantum wells and coupled superlattices. The superlattices are treated within the anisotropic medium approach, in which the motion of electrons and holes is characterized by in-plane and transverse effective masses.[7,8] On the other hand, for quantum wells, we solve the Luttinger Hamiltonian in order to obtain the multliple-coupled-subband dispersion relations and dipole moments used as input for our Green's functions calculations.[9,5] However, we consider static screening in the dephasing computations. Figure 1 displays the RPA dephasing of electrons obtained from the imaginary part of the corresponding retarded selfenergy for a II-VI superlattice. Higher order corrections are due to T-matrix corrections and are depicted in Fig. 2. The RPA dephasing follows the electronic dispersion, while the T-matrix dephasing is centered about the excitonic dispersion. Figure 3 illustrates the excitonic bleaching at the T-matrix level for a 15$\mathring{A}$ / 5$\mathring{A}$ GaAs superlattice at 150 K. As the carrier density increases from N = 10^{13} to 10^{18} *carriers/cm*^{3}, the Coulomb enhancement evolves from excitonic features about the exciton binding energies to a correction about the electronic dispersion. Figure 4 shows distribution functions for a 5$\mathring{A}$ / 75$\mathring{A}$ ZnSe-ZnMgSe superlattice. The top, central and lower plots are, respectively for T = 77, 150 and 300K. On the left and right, N = 10^{15}, and 10^{16} *carriers/cm*^{3}. The solid, dot-dashed curves are respectively for Fermi and exciton distributions. The circles depict the Wigner distributions. Here, the exciton distributions are defined as the convolution of the squared 1s wavefunction with the center-of-mass Boltzmann distribution. Note that, as the temperature increases, the Fermi and Wigner distributions are indistinguishable. In other words, in this case, we can compute optical spectra without the T-matrix diagram in the carriers self-energy. Figure 5 displays the optical absorption with the T-matrix included on both polarization and self-energy diagrams. In 75$\mathring{A}$ barrier SL, there is larger electron-hole overlap in the well region giving rise to larger oscillator strength for the optical transition and requiring a larger carrier density to bleach the exciton. Note further that the abscissae are normalized to the effective Rydberg, which is accordingly larger in the 75$\mathring{A}$ case.
The results for isolated QW's are for high temperatures, and we can thus use RPA dephasing only. Figure 6 shows the computed modal gain (negative absorption) for a series of ZnSe/(Zn,Mg)(S,Se) single quantum wells with different well widths at 200 K, while results for 300 K are given in Figure 7. The optical confinement factors for the 70,50, and 30 $\mathring{A}$ QW's structures are given respectively, by 0.029, 0.021 and 0.013. Several subbands contribute to the gain spectra at high carrier densities. Note that, the larger the subband separation from the band-edge, the smaller the carrier occupation and thus, as Eq. 21 indicates through the subband label dependence, the smaller the corresponding dephasing. Consequently, the corresponding contribution to the gain leads to sharper structures. Figure 8 compares the widths and strengths of the different transitions for 70 $\mathring{A}$ QW. For larger well widths, were the EE2-HH2 transition gives a larger contribution to the higher order gain structures, the transition is even sharper.
The spectral position of the different subband structures is in good agreement with recent experimental data,[10] which further supports our interpretation of the high-temperature gain mechanism as the recombination of a strongly-interacting electron hole plasma. As the temperature is further reduced, T-matrix and higher order effects (that reduce to biexcitonic form under limiting cases) play an increasingly important role.
In summary, the microscopic theory for the nonlinear optical properties of semiconductors presented here provides a

technique to study Coulomb effects beyond RPA, by analysing their influence on optical spectra. Unphysical features, like a spurious absorption for photon frequencies below those in the gain range do not appear, since our polarization function satisfies the KMS sum rule. The numerical results show that the actual carrier occupation functions (Wigner distributions) differ from the commonly used Fermi distributions for sufficiently low carrier densities and temperatures. Our iterated RPA and T-matrix dephasing adds further predictability to the approach and for multi-subband quantum wells provides important insight on high- density gain operation, which may be important for high-power semiconductor laser applications. The approach presented can also be used as the starting point for the realistic simulation of more complicated light-emitting and processing devices.

REFERENCES

1. R. Zimmermann, *Many-Particle Theory of Highly Excited Semiconductors*, Teubner, Leipzig, 1988.
2. H. Haug and S. Koch, *Quantum Theory of the Optical and Electronic Properties of Semiconductors*, World Scientific, Singapore, 1990.
3. M. Pereira Jr., S. Koch, and W. Chow, "Effects of strain and coulomb interaction on gain and refractive index in quantum well lasers," *J. Opt. Soc. Am. B* **10**, p. 765, 1993.
4. R. Schepe, T. Schmielau, D. Tamme, and K. Henneberger, "Damping and T-Matrix in dense e-h plasmas," *phys. stat. sol. (b)* **206**, pp. 273–279, 1998.
5. M. Pereira Jr. and K. Henneberger, "Microscopic theory for light-emission in coulomb correlated semiconductor quantum wells," *Phys. Rev. B* **58**, pp. 2064–2076, 1998.
6. K. Henneberger and H. Haug, "Nonlinear optics and transport in laser-excited semiconductors," *Phys. Rev. B* **38**, pp. 9759–9770, 1988.
7. M. Pereira Jr., I. Galbraith, S. Koch, and G. Duggan, "Exciton binding energies in semiconductor superlattices: An anisotropic effective-medium approach," *Phys. Rev. B* **42**, pp. 7084–7089, 1990.
8. M. Pereira Jr., "Analytical solutions for the optical absorption of superlattices," *Phys. Rev. B* **52**, pp. 1978–1983, 1995.
9. M. Pereira Jr. and K. Henneberger, "Green's functions theory for semiconductor quantum well laser," *Phys. Rev. B* **53**, pp. 16485–16496, 1996.
10. P. Michler, M. P. Jr, O. Homburg, L. Nerger, J. Gutowski, H. Wenisch, and D. Hommel, "Gain characteristics of znse/(zn,mg)(s,se)/(zn,mg)(s,se) quantum well lasers," *Physics and Simulation of Optoelectronic Devices* **Proc. SPIE**, p. 3625, 1999.

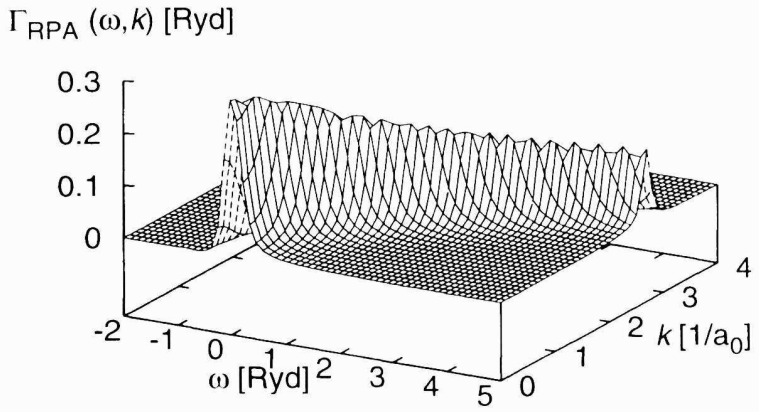

Figure 1. RPA dephasing for a 5 A ZnSe / 75 A ZnMgSe superlattice at T=77K and n = $10^{15} carriers/cm^3$.

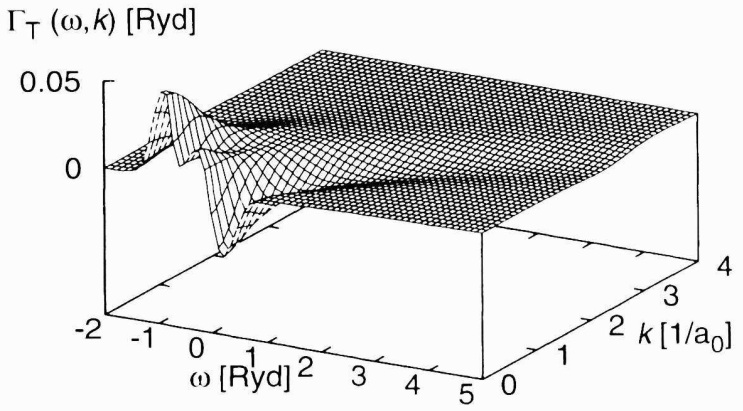

Figure 2. T-matrix dephasing for the superlattice of Fig. 2 with the same parameters.

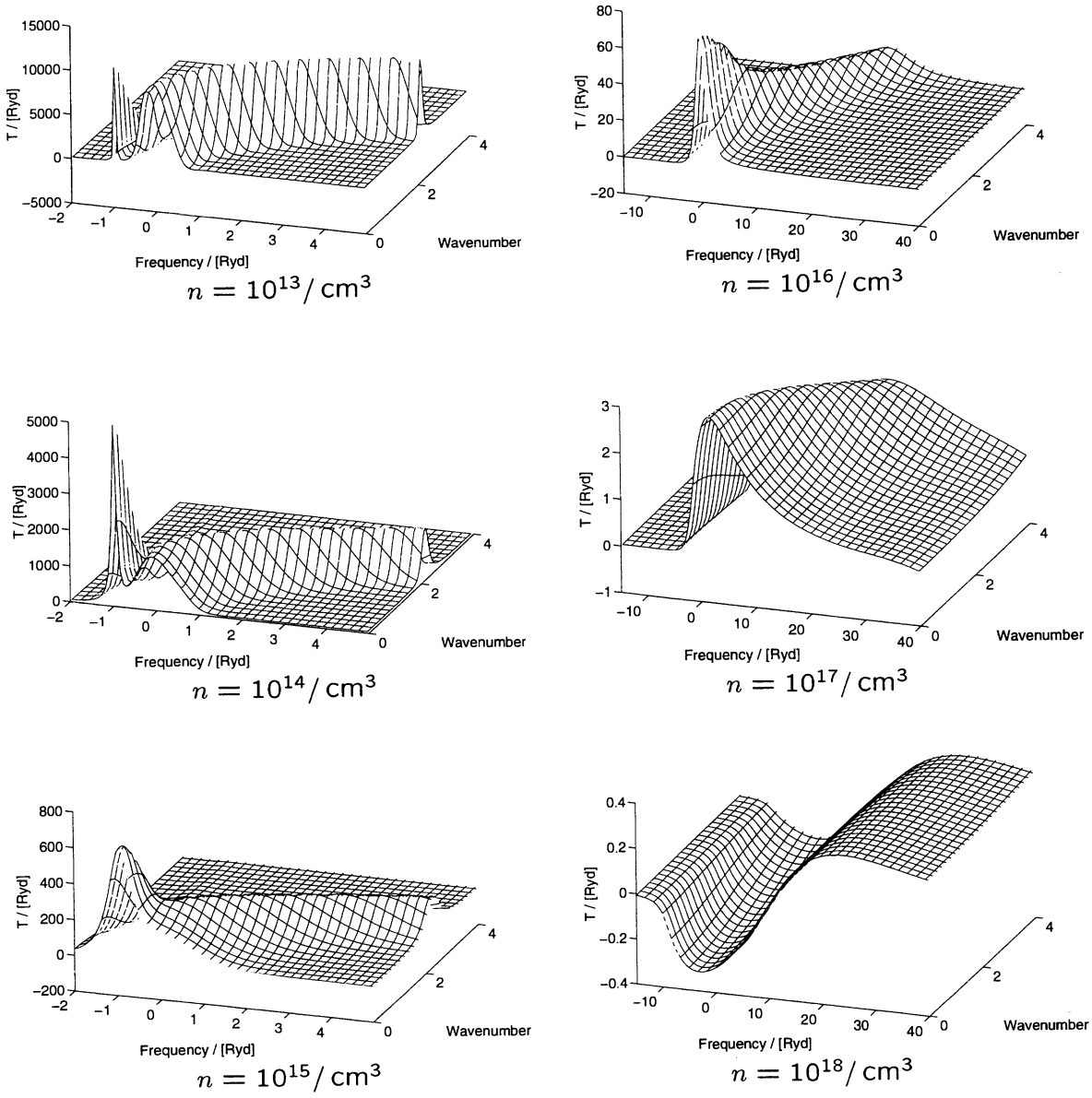

Figure 3. Evolution with increasing temperature of the T-matrix for a 15Å GaAs / 5Å$Al_{0.23}Ga_{0.77}$ As superlattice.

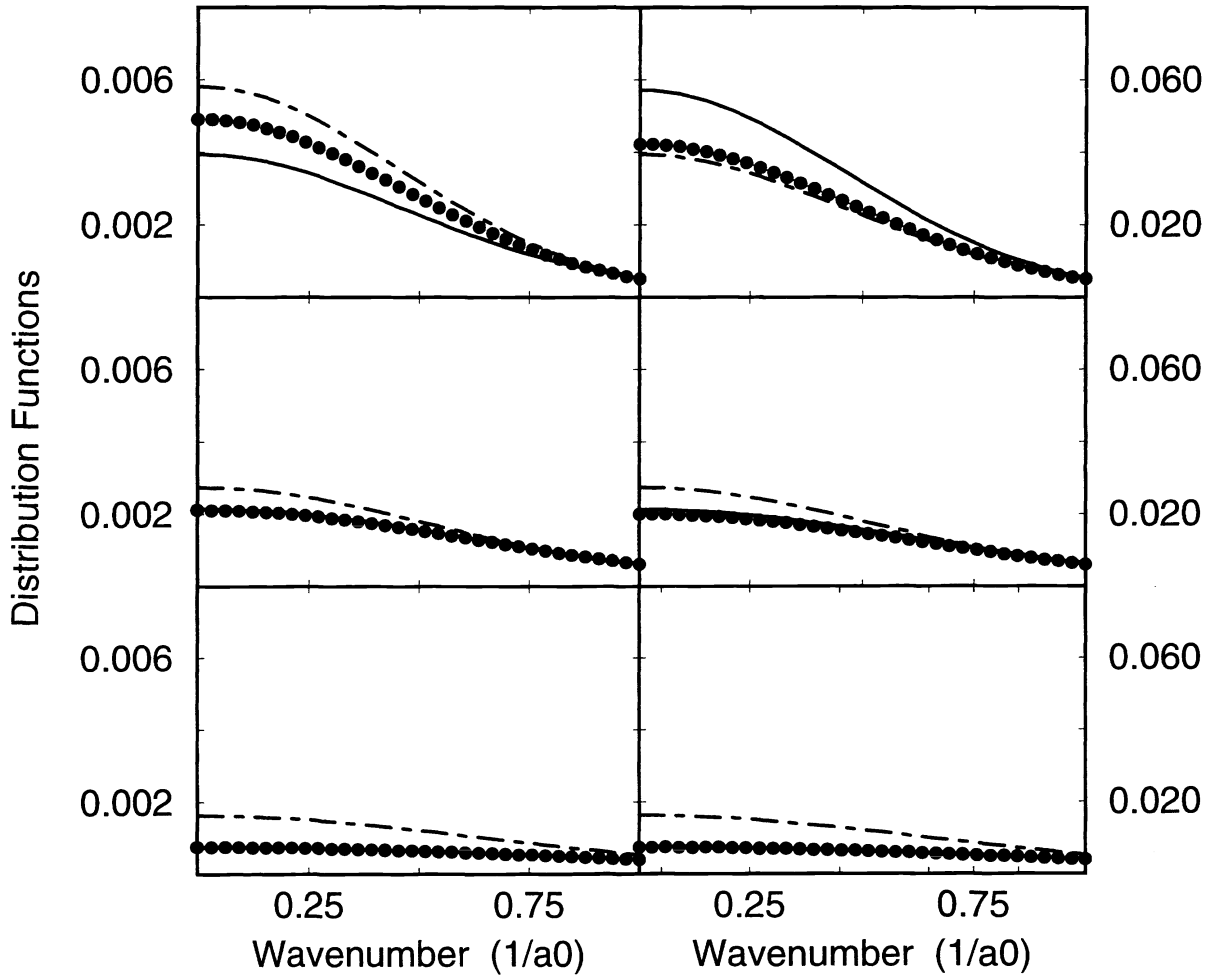

Figure 4. Distributions functions for a $5\mathring{A}$ / $75\mathring{A}$ ZnSe-ZnMgSe superlattice. The top, central and lower plots are, respectively for T = 77, 150 and 300K. On the left and right, N = 10^{15}, and 10^{16} $carriers/cm^3$. Solid: Fermi distributions; Dot-dashed: Exciton distributions; Circles: Wigner distributions.

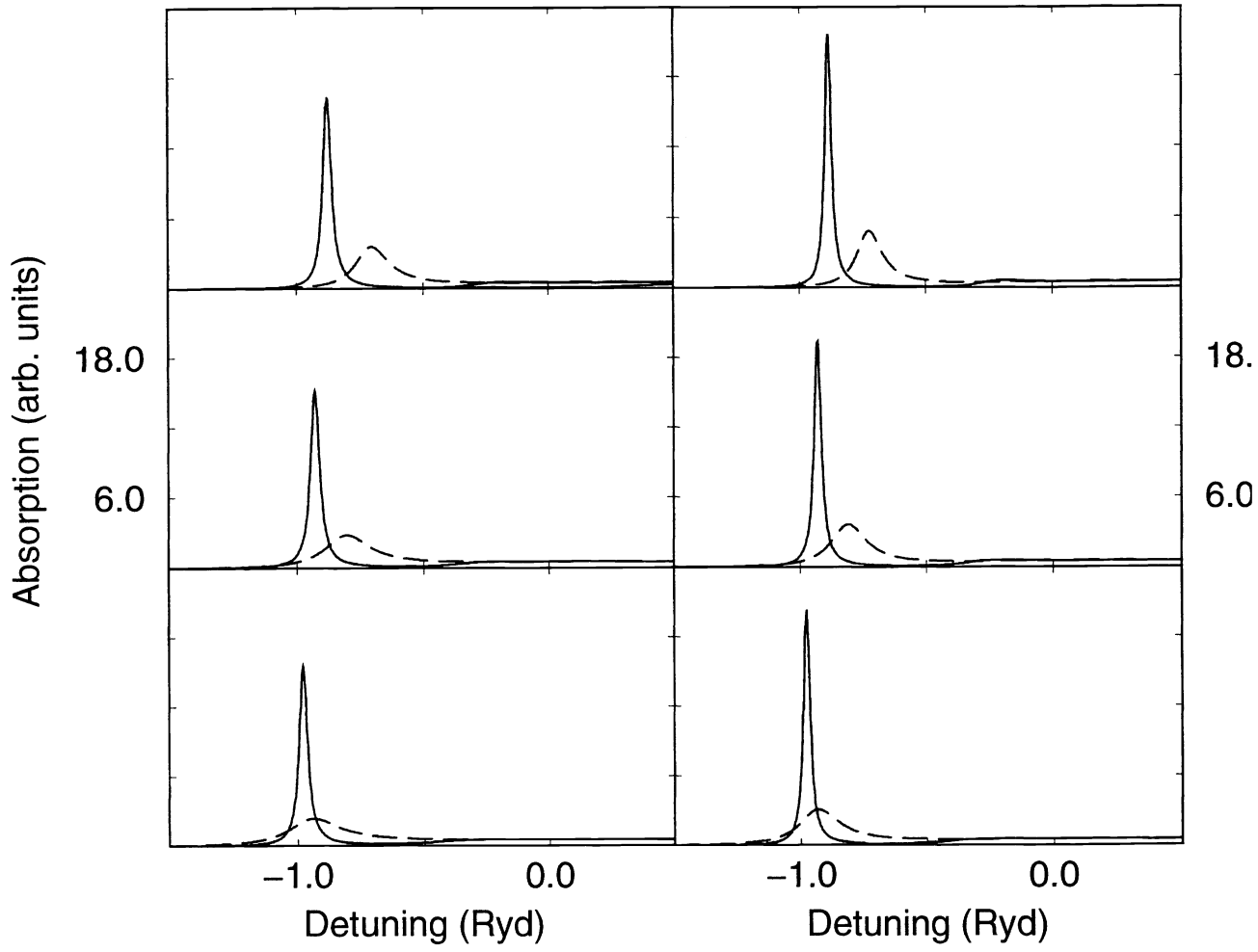

Figure 5. Optical absorption for 15 $\AA$ / 5 $\AA$ (left), and 15 $\AA$ / 75 $\AA$ (right) ZnSe-ZnMgSe superlattices. The top, central and lower plots are, respectively for T = 77, 150, and 300K. On the left and right, The solid and dashed curves are, respectively, for N = 10^{15}, and 10^{16} $carriers/cm^3$.

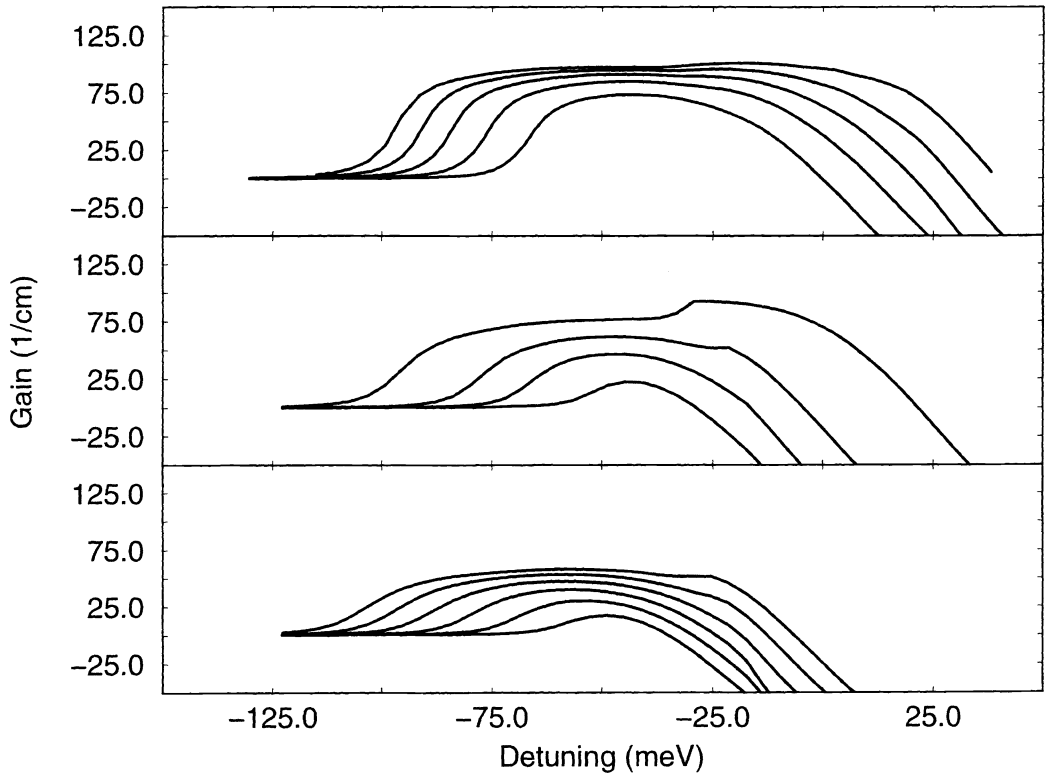

Figure 6. Modal optical gain at 200 K for 70, 50 and 30 $\AA$ ZnSe-ZnMgSe QW'S (top, middle, bottom). From top to bottom the carrier densities are N = 14,12,10,8,6 x 10^{16} $carriers/cm^3$, (70 $\AA$). N = 14,12,8,6,4 x 10^{16} $carriers/cm^3$, (50 $\AA$). N = 16,14,12,10,8,6 x 10^{16} $carriers/cm^3$.

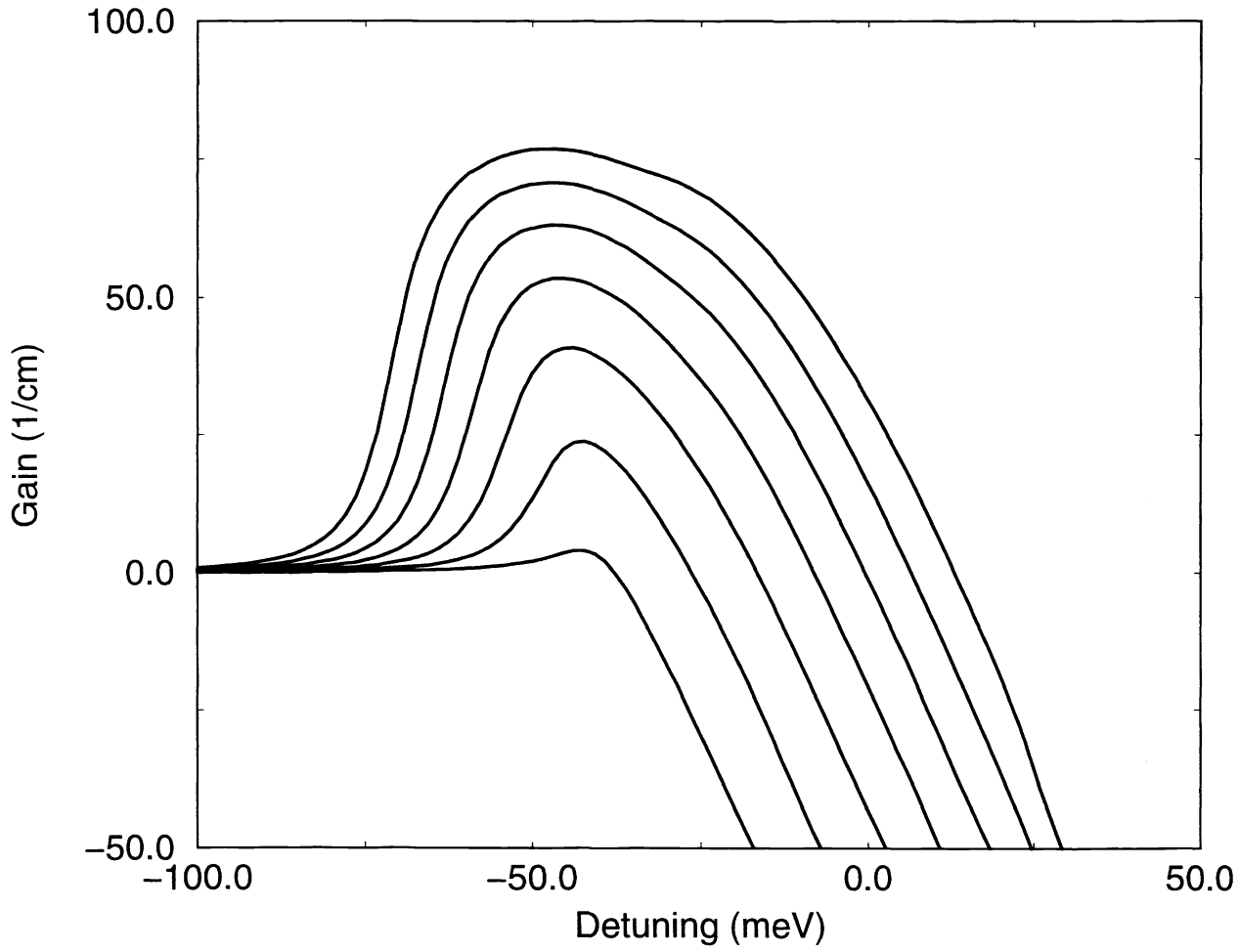

Figure 7. Modal optical gain for a 70 $\AA$ ZnSe-ZnMgSe quantum well at 300K. From top to bottom the carrier densities are N = 10,9,8,7,6,5,4 $\times$ 10^{16} $carriers/cm^3$.

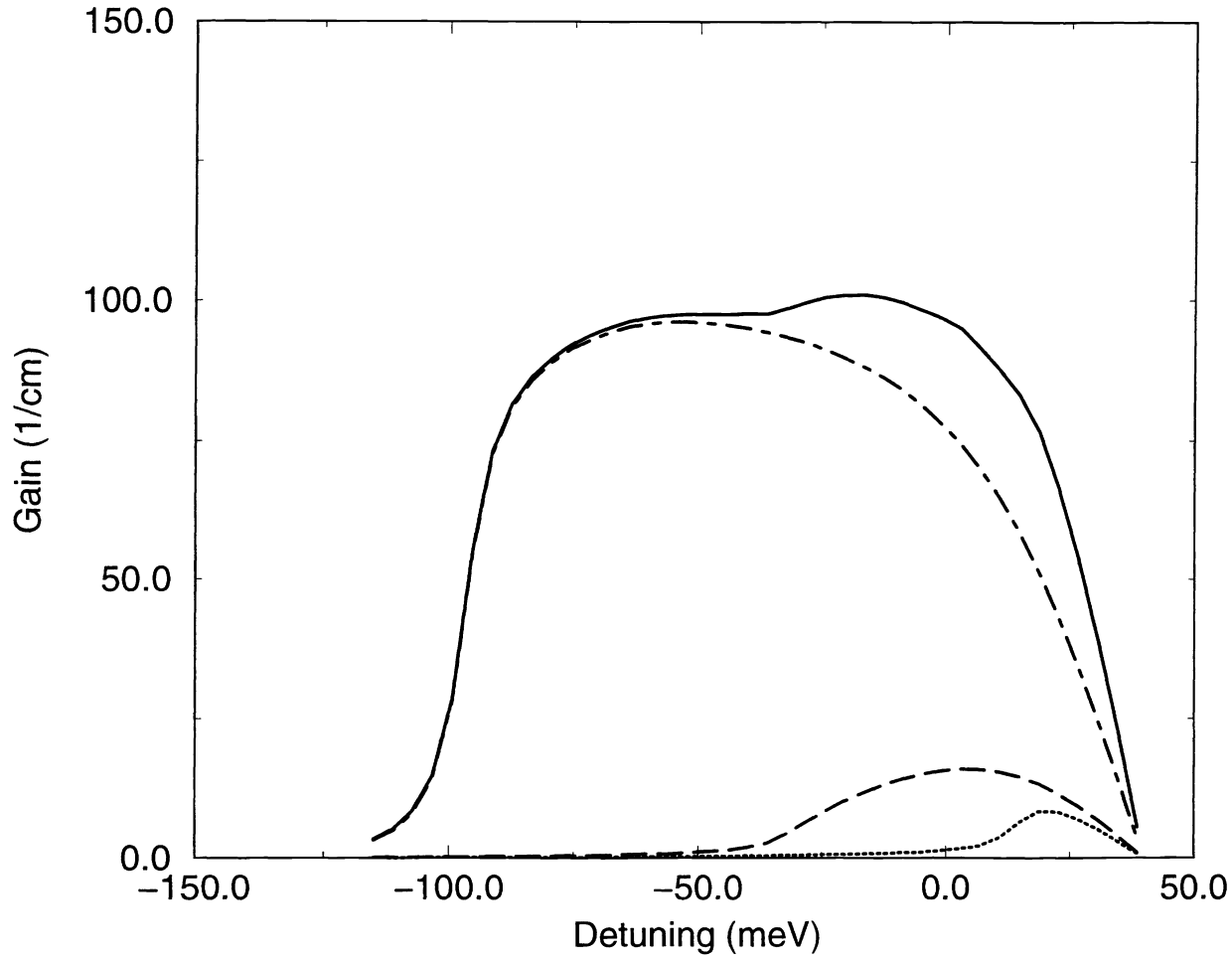

Figure 8. Modal optical gain at 200 K for a 70 $\AA$ QW: The transitions considered that add up to make the final (solid) curve are: E1-HH1 (dot-dashed), E1-HH2 (dashed), (E2-HH2) (dotted).